ChemComm

Chemical Communications

Accepted Manuscript

This article can be cited before page numbers have been issued, to do this please use: X. Huang, S. Zhang, K. Xu, Y. Hu, Y. Li, W. Feng, H. GONG, Y. Pi, T. Tian and H. Pang, *Chem. Commun.*, 2025, DOI: 10.1039/D5CC02629F.

ChemComm

View Article Online
DOI: 10.1039/D5CC02629F

COMMUNICATION

2D Boehmite/Mesoporous Nanosphere Composites with Hierarchical Ion Transport for Efficient Capacitive Deionization

Received 00th January 20xx,
Accepted 00th January 20xx

DOI: 10.1039/x0xx00000x

Xingyu Huang,[a] Songtao Zhang,[a] Kun Xu,[a,b] Yaxun Hu,[a] Yong Li,[a,c] Wanchang Feng,[a] Hao Gong,[d] Yecan Pi,[a] Tian Tian [a] and Huan Pang *[a,e]*

Mesoporous nanospheres coated with 2D Boehmite nanosheets were synthesized. The hierarchical ion-transport networks within this engineered structure facilitate efficient Na^+ transport. The optimized composite exhibits a high salt adsorption capacity (131.3 mg g^{-1}, 1.2 V) and good regenerative stability (93.5%). Advances composite materials design for desalination technologies.

The increasing energy shortage and growing need for freshwater have made seawater desalination a key research topic.[1, 2] Capacitive deionization (CDI) is a sustainable solution owing to its low energy consumption and regeneration efficiency. Conventional carbon electrodes for CDI application are hindered by sluggish ion transport.[3] Various hierarchical porous materials with tailored architectures have been developed to enhance ion accessibility.[4, 5] Polydopamine (PDA)–derived mesoporous carbons feature hierarchical porosity and excellent stability. However, it still suffers from interfacial kinetic barriers.[6, 7] Ultrathin alumina-modified composites have been found to enhance ion-transport rates while preserving substrate stability.[8, 9] Herein, ultrathin boehmite nanosheet-coated PDA composites are synthesized via hydrothermal deposition and carbonization. Trimesic acid (BTC) and aluminum precursor ratios were adjusted to precisely control the boehmite thickness. This adjustment could generate permeable channels that accelerate Na^+ migration.[10]

Highly uniform mesoporous PDA nanospheres (mesoPDA-F127) were synthesized through 1,3,5-trimethylbenzene-mediated interfacial interactions between Pluronic F127 and dopamine.[11] A one-pot hydrothermal process was used to integrate a thickness-tunable boehmite coated on the precursor mesoPDA-F127. This process involved systematically regulating the contents of BTC and aluminum precursors to achieve homogeneous coating on the PDA nanospheres. The resulting composites are designated as mesoPDA-F127/AlO(OH)-x, where x represents different precursor ratios (Tab. S1, ESI†). The composite precursor was calcined at 700 °C, producing N-doped porous carbon nanospheres coated with Al_2O_3 nanosheet (mesoPDA-F127/AlO(OH)-x-700) (Fig. 1a).

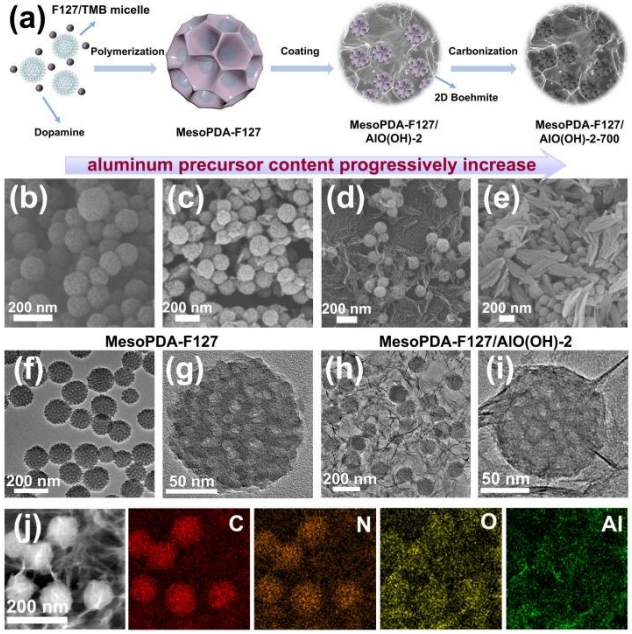

Fig. 1 (a) Synthesis scheme. SEM images of (b) mesoPDA-F127, (c) mesoPDA-F127/AlO(OH)-1, (d) mesoPDA-F127/AlO(OH)-2, and (e) mesoPDA-F127/AlO(OH)-3. TEM images of (f, g) mesoPDA-F127 and (h, i) mesoPDA-F127/AlO(OH)-2. (j) Elemental mapping of mesoPDA-F127/AlO(OH)-2.

[a] School of Chemistry and Chemical Engineering, Testing Center, Yangzhou University, Yangzhou, 225009, P. R. China.
[b] School of Environmental Science, Nanjing Xiaozhuang University, Nanjing, Jiangsu, 211171, P. R. China.
[c] College of Chemistry and Chemical Engineering, Chongqing University of Science and Technology, Chongqing, 401331, P. R. China.
[d] Department of Chemistry and Materials Science, College of Science, Nanjing Forestry University, Nanjing 210037, P. R. China.
[e] State Key Laboratory of Coordination Chemistry, Nanjing University, Nanjing 210023, P. R. China.
† Email: zhangsongtao@yzu.edu.cn (Songtao Zhang); huanpangchem@hotmail.com, panghuan@yzu.edu.cn (Huan Pang)
Supplementary Information available: See DOI: 10.1039/x0xx00000x

The surface microstructures of mesoPDA-F127 and composites mesoPDA-F127/AlO(OH)-x has been studied using scanning electron microscopy (SEM). The mesoPDA-F127 nanospheres exhibit uniform porous architecture with well-defined spherical morphology (Fig. 1b). A distinct nanosheet grows on the surface of mesoPDA-F127/AlO(OH)-x nanospheres, and the thickness of the nanosheet changes significantly with different precursor ratios increase (Fig. 1c-1e and Fig. S1, ESI†). The morphology of the synthesized nanospheres was further analyzed using transmission electron microscopy (TEM) (Fig. 1f-1i and Fig. S2, ESI†). The monodisperse nanospheres with an average diameter of 140 nm were observed. The mesoPDA-F127/AlO(OH)-2 nanospheres featured a uniformly distributed boehmite layer with an optimal thickness. In the absence of BTC, sporadic flake-like deposits appeared on the nanosphere surfaces. In contrast, it can be found that excessive BTC concentrations induced undesirable nanosheet thickening.

High-resolution transmission electron microscopy (HRTEM) of mesoPDA-F127/AlO(OH)-2 (Fig. S3, ESI†) revealed that the nanosheets on the mesoporous spheres possess a 2D morphology without discernible lattice fringes. Morphological characterization of calcined mesoPDA-F127-700 and mesoPDA-F127/AlO(OH)-2-700 was also performed (Fig. S4, ESI†). Significant morphological evolution was observed in mesoPDA-F127-700, characterized by nanosphere shrinkage and localized aggregation. This phenomenon is most likely attributed to solvent evaporation and subsequent cross-linking reactions, which collectively induce the framework contraction.[12] The mesoPDA-F127/AlO(OH)-2-700 composite also exhibited a noticeable degree of size contraction compared to its precursor. The EDS elemental mapping analysis of mesoPDA-F127/AlO(OH)-2 (Fig. 1j) reveals the homogeneous distribution of carbon, oxygen, and nitrogen across the nanospheres. Al species come from the surface-loaded thin nanosheet architecture. These results confirm the successful integration of nanosheet structures onto PDA nanosphere surfaces.

X-ray diffraction (XRD) analysis of mesoPDA-F127 and mesoPDA-F127/AlO(OH)-x (Fig. 2a) revealed a broad peak centered at 2θ around 23°, characteristic of disordered carbon structures typically observed in PDA-derived materials.[13] The progressive enhancement of aluminum precursor content induced intensified characteristic diffraction peaks corresponding to the orthorhombic AlO(OH) phase (JCPDS card No.83-2384). The peak locations are observed at 2θ around 14.49°, 28.21°, 38.36°, and 48.94°, which were systematically indexed to the (020), (120), (031), and (051) crystallographic planes, respectively. The analysis showed clear changes in the crystal structure caused by heating (Fig. S5a, ESI†). Two diffraction peaks located at 2θ around 24° and 43° of mesoPDA-F127-700 are identified as typical (002) and (100) diffraction peaks of amorphous carbon framework.[14] For mesoPDA-F127/AlO(OH)-2-700, in addition to a carbon peak at 24.06°, there are two peaks near 45.91° and 66.95°, belonging to the (200) and (220) crystal planes, respectively. This is consistent with the cubic crystalline structure of $(Al_2O_3)_{1.333}$ (JCPDS card No.75-0921).

The pore structures of mesoPDA-F127 and mesoPDA-F127/AlO(OH)-2 were systematically analysed using nitrogen adsorption-desorption measurements (Fig. 2b). Both materials exhibited type IV isotherms, indicative of well-developed mesoporous structures. Remarkably, mesoPDA-F127/AlO(OH)-2 demonstrated a substantially enhanced specific surface area of 112.47 $m^2 g^{-1}$ compared to pristine mesoPDA-F127 (42.16 $m^2 g^{-1}$) (Fig. S5b and Tab. S2, ESI†), such an increase could be associated with the formation of boehmite nanosheet coatings on the nanospheres surface.[15] Importantly, mesoPDA-F127/AlO(OH)-2 showed a smaller average pore size. This confirms that boehmite incorporation induced pore contraction. Thermogravimetric analysis (TGA) profiling substantiates the decomposition of the polymeric template (Pluronic F127) below 400 °C.[16] At 700 °C, mesoPDA-F127 retains about 51.69% of its carbon content (Fig. 2c). The carbonization efficiency of mesoPDA-F127/AlO(OH)-2 (61.33%) is higher than that of mesoPDA-F127, indicating better structural stability during thermal processing. Fourier transform infrared (FT-IR) analysis (Fig. 2d) revealed the disappearance of specific functional groups in mesoPDA-F127 following composite formation. Peaks observed at 480, 631, 1065, and 1638 cm^{-1} were attributed to newly formed AlO(OH) structural features,[17] while the 1485 cm^{-1} peak corresponded to benzene ring stretching vibrations.[18, 19] These spectral changes confirm the successful synthesis of the composite material.

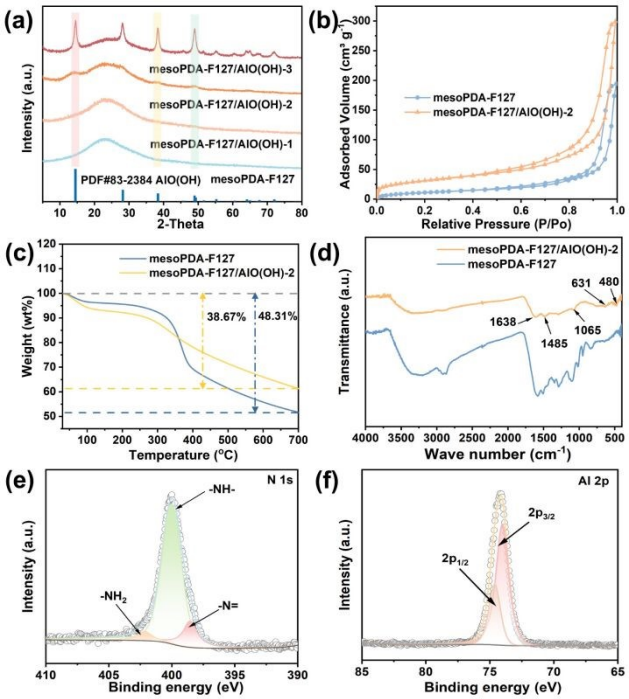

Fig. 2 (a) XRD patterns. (b) N_2 adsorption/desorption isotherms. (c) TGA curves under N_2 flow (10 °C min^{-1}). (d) FT-IR spectra. High-resolution XPS spectra of mesoPDA-F127/AlO(OH)-2: (e) N 1s and (f) Al 2p.

X-ray photoelectron spectroscopy (XPS) confirmed the elemental composition and chemical states in mesoPDA-F127 and mesoPDA-F127/AlO(OH)-2 (Fig. 2e-2f and Fig. S6, ESI†). The survey spectrum of mesoPDA-F127 reveals C, O, and N signals with no impurities. The C 1s spectra for both materials

deconvolute to three components: C-C, C-N/C-O, and O-C=O. Similarly, N 1s spectra display three distinct states (-N=, -NH-, and -NH_2),[20] while O 1s spectra show contributions from C=O and C-O bonds. Notably, mesoPDA-F127/AlO(OH)-2 exhibits additional Al 2p peaks which can be ascribed to the Al-O bond.[21, 22] Composite formation induces a positive shift in N 1s and a negative shift in O 1s binding energies, indicating a modified coordination environment (Tab. S3, ESI†). These results highlight the successful integration of the Al-O bond into the carbon framework, enhancing interfacial interactions.

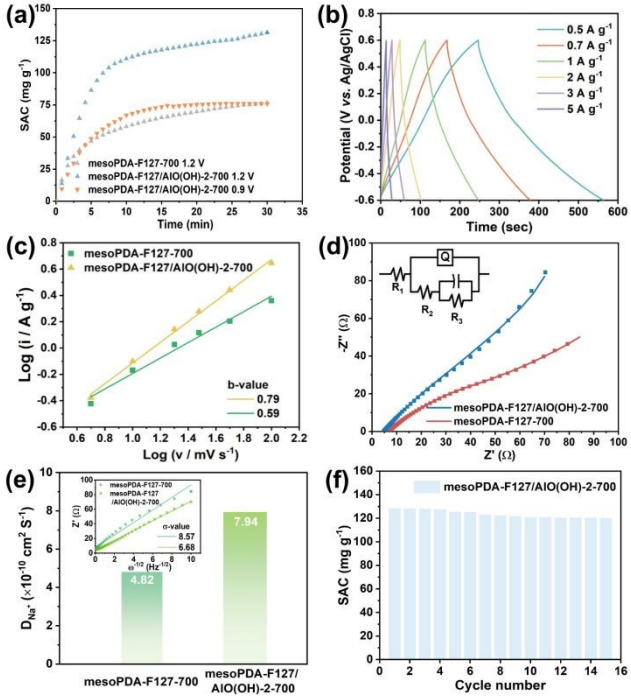

Fig. 3 CDI performance at 1.2 V (10 mM NaCl): (a) Deionization capacity. (b) GCD curves (1 M NaCl). (c) Linear fitting of the charging process. (d) EIS plots. (e) Na^+ diffusion coefficient. (f) Desalination regeneration cycling.

To systematically evaluate desalination performance, CDI experiments were performed on mesoPDA-F127-700 and mesoPDA-F127/AlO(OH)-2-700 under controlled electrochemical conditions (Fig. 3a). The mesoPDA-F127/AlO(OH)-2-700 electrode exhibited a substantially enhanced salt adsorption capacity (SAC) of 131.3 mg g^{-1} at the voltage of 1.2 V, representing a 71.6% improvement over the pristine mesoPDA-F127-700 electrode (76.5 mg g^{-1}). This improvement shows that nanosheet structure design plays a key role in enhancing CDI efficiency. Systematic evaluation of voltage-dependent behavior revealed that the mesoPDA-F127/AlO(OH)-2-700 composite maintained a SAC of 75.9 mg g^{-1} at 0.9 V, attaining equality with the mesoPDA-F127-700 baseline performance at 1.2 V. This demonstrates that mesoPDA-F127/AlO(OH)-2-700 can retain high desalination capacity under reduced voltage, a critical factor for lowering energy consumption in practical CDI applications.[23] Besides, the SAC of mesoPDA-F127/AlO(OH)-2-700 electrode (131.3 mg g^{-1}) is notably higher than that of previously reported PDA-derived composites (12.95 mg g^{-1}) (Tab. S4, ESI†). From the Ragone plots of the CDI system (Fig. S7, ESI†), it can be found that the mesoPDA-F127/AlO(OH)-2-700 showed better desalting capability than mesoPDA-F127-700. To further investigate the electrochemical characteristics of the materials, cyclic voltammetry (CV) measurements were conducted using a three-electrode system (Fig. S8, ESI†). Within the applied potential, the mesoPDA-F127/AlO(OH)-2-700 electrode demonstrated favorable capacitive behavior without distinct redox peaks. A comparative analysis of the CV curves showed that mesoPDA-F127/AlO(OH)-2-700 exhibited a significantly larger enclosed area than its pristine counterpart, suggesting superior charge storage performance.[24-26] The charge-discharge characteristics of the three-electrode system were systematically investigated across varying current densities (Fig. 3b and Fig. S9, ESI†). The discharge duration of the electrode exhibits a positive correlation with its specific capacitance (Eq. S1, ESI†). At 1 A g^{-1}, the mesoPDA-F127/AlO(OH)-2-700 electrode exhibited an extended discharge time of 135 s compared to mesoPDA-F127-700 (99 s), indicating accelerated ion storage and release kinetics. The mesoPDA-F127/AlO(OH)-2-700 electrode also kept high specific capacitance at different current densities. These results are consistent with the CV measurements.

Linear analysis of the charging process yielded a characteristic b-value of 0.79 for the mesoPDA-F127/AlO(OH)-2-700 electrode (Eq. S2-3, ESI†). This suggests a hybrid charge storage mechanism driven by the synergistic contributions of diffusion-controlled ion transport and surface-induced capacitive processes (Fig. 3c). In contrast, the pristine mesoPDA-F127-700 electrode demonstrated b-values closer to 0.5 across various scan rates, indicating a predominantly diffusion-controlled charge storage mechanism governed by ion intercalation dynamics.[27] The relative percentages of pseudo-capacitive and diffusion-controlled contributions were quantified (Eq. S4-5, ESI†). At a scan rate of 100 mV s^{-1}, the mesoPDA-F127/AlO(OH)-2-700 electrode exhibited a capacitive contribution of 64.79%, notably higher than that of the pristine mesoPDA-F127-700 electrode (42.22%) (Fig. S10, ESI†). Charge transfer kinetics at the electrode-electrolyte interface were analyzed using electrochemical impedance spectroscopy (EIS). The mesoPDA-F127/AlO(OH)-2-700 electrode exhibited a near-vertical shape in the Nyquist plot (Fig. 3d), indicating a rapid ion diffusion kinetics and ideal capacitive behavior.[28] It exhibited a lower charge transfer resistance (4.75 Ω) compared to the pristine electrode (6.67 Ω) (Table S5, ESI†). Sodium ion diffusion coefficients (D_{Na^+}) and diffusion resistances (ϕ) were calculated through Nyquist curve fitting (Eq. S6-7, ESI†). Remarkably, mesoPDA-F127/AlO(OH)-2-700 demonstrated a lower diffusion resistance (6.68 Ω) and higher sodium ion diffusivity (7.94×10^{-10} cm^2 s^{-1}) compared to mesoPDA-F127-700 (8.57 Ω, 4.82×10^{-10} cm^2 s^{-1}) (Fig. 3e). These comprehensive analyses confirm the reversible and rapid Na^+ storage capability of mesoPDA-F127/AlO(OH)-2-700 electrode (Table S6, ESI†). Systematic cycling tests were conducted to evaluate the material's desalination stability (Fig. 3f). The composite retained an adsorption capacity of 120.1 mg g^{-1} after 15 cycles. This corresponds to 93.5% retention of its initial value, indicating good cycling durability for CDI applications.

DFT calculations were performed to evaluate Na^+ adsorption on N-doped graphene and alumina models (Fig. S11, ESI†). Besides, charge density maps visualize electron redistribution during adsorption (Fig. 4a-b). It can be found that the model of alumina (-3.60 eV) has much lower adsorption energy than N-doped graphene (-0.90 eV) (Fig. 4c and Eq. S8, ESI†), which indicates that alumina material has a better thermodynamic adsorption capacity for Na^+.[29] It can be seen that loading alumina nanosheets significantly enhances Na^+ adsorption on N-doped mesoporous carbon.

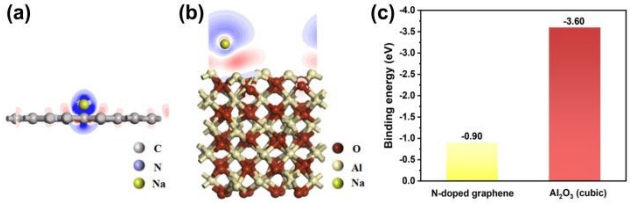

Fig. 4 Charge density difference for Na^+ adsorption on (a) N-doped graphene and (b) alumina (cubic). (c) Energy difference of Na^+ adsorption in different models.

In summary, a facile synthesis of mesoporous carbon nanospheres with tunable 2D boehmite coatings is achieved via controlled precursor ratios. The composite exhibits an increased specific surface area and synergistic Al_2O_3-carbon interfacial interactions. The optimized mesoPDA-F127/AlO(OH)-2-700 electrode delivers a good desalination capacity of 131.3 mg g^{-1} (1.2 V) while retaining 93.5% capacity over regeneration cycling. Theoretical calculations reveal that the layer of alumina nanosheet significantly enhances Na^+ adsorption in N-doped carbon frameworks. This study advances composite materials design toward next-generation desalination materials.

This work was supported by the National Natural Science Foundation of China (52371240) and the Priority Academic Program Development of Jiangsu Higher Education Institutions.

Conflicts of interest

There are no conflicts to declare.

Data availability

The data supporting this article have been included as part of the Supplementary Information.

Notes and references

1 M. M. Mekonnen and A. Y. Hoekstra, *Sci. Adv.*, 2016, **2**, e1500323.
2 Y. Ham, N. J. Fritz, G. Hyun, Y. B. Lee, J. S. Nam, I.-D. Kim, P. V. Braun and S. Jeon, *Energy Environ. Sci.*, 2021, **14**, 5894-5902.
3 S. Zhang, M. Zheng, Y. Tang, R. Zang, X. Zhang, X. Huang, Y. Chen, Y. Yamauchi, S. Kaskel and H. Pang, *Adv. Funct. Mater.*, 2022, **32**, 2204714.
4 J. Wang, S. Qu, R. Zhang, K. Yang, S. Zhang, R. G. Nuzzo, J. Nanda and P. V. Braun, *Energy Technol.*, 2021, **9**, 2100175.
5 Z. Yu, J. Wang, N. Zhang, J. Shin, Q. Zheng, S. Qu, X. He, A. Rockett, H. Yang and P. V. Braun, *RSC Adv.*, 2018, **8**, 38745-38750.
View Article Online
DOI: 10.1039/D5CC02629F
6 J. Li, R. Wang, L. Han, T. Wang, Y. Asakura, C. Wang, G. Wang, X. Xu and Y. Yamauchi, *Nat. Commun.*, 2025, **16**, 1996.
7 S. Zhang, Y. Li, X. Zhuang, Y. Hu, K. Xu, G. Zhang, Y. Pi, Y. Tang, J. Hu, R. Zang, Z. Qiu, H. Zhou, F. Yu, M. Shakouri and H. Pang, *Adv. Mater.*, 2025, **37**, 2418344.
8 X. Hu, M. Jing, H. Yang, Q. Liu, F. Chen, W. Yuan, L. Kang, D. Li and X. Shen, *J Colloid Interf. Sci.*, 2021, **590**, 50-59.
9 P. Liu, H. Hao, A. Singla, B. S. Vishnugopi, J. Watt, P. P. Mukherjee and D. Mitlin, *Angew. Chem. Int. Ed.*, 2024, **63**, e202402214.
10 R. Fang, Y. Li, N. Wu, B. Xu, Y. Liu, A. Manthiram and J. B. Goodenough, *Adv. Funct. Mater.*, 2023, **33**, 2211229.
11 L. Peng, H. Peng, W. Li and D. Zhao, *Nat. Protoc.*, 2023, **18**, 1155-1178.
12 Y. Fang, Y. Lv, F. Gong, Z. Wu, X. Li, H. Zhu, L. Zhou, C. Yao, F. Zhang, G. Zheng and D. Zhao, *J. Am. Chem. Soc.*, 2015, **137**, 2808-2811.
13 P. Lu, Y. Sun, H. Xiang, X. Liang and Y. Yu, *Adv. Energy Mater.*, 2018, **8**, 1702434.
14 Y. Tang, Y. Shi, Y. Su, S. Cao, J. Hu, H. Zhou, Y. Sun, Z. Liu, S. Zhang, H. Xue and H. Pang, *Adv. Sci.*, 2024, **11**, 2403802.
15 Z. Yang, L. Jin, G. Lu, Q. Xiao, Y. Zhang, L. Jing, X. Zhang, Y. Yan and K. Sun, *Adv. Funct. Mater.*, 2014, **24**, 3917-3925.
16 L. Peng, C. Hung, S. Wang, X. Zhang, X. Zhu, Z. Zhao, C. Wang, Y. Tang, W. Li and D. Zhao, *J. Am. Chem. Soc.*, 2019, **141**, 7073-7080.
17 M. Abdollahifar, R. M. Zamani, E. Beiygie and H. Nekouei, *J. Serb. Chem. Soc.*, 2014, **79**, 1007-1017.
18 Y. Cao, H. Fang, C. Guo, W. Sun, Y. Xu, Y. Wu and Y. Wang, *Angew. Chem. Int. Ed.*, 2023, **62**, e202302143.
19 X. Zhang, K. Yue, R. Rao, J. Chen, Q. Liu, Y. Yang, F. Bi, Y. Wang, J. Xu and N. Liu, *Appl. Catal. B Environ.*, 2022, **310**, 121300.
20 Y. Ai, C. Yang, Z. Yin, T. Wang, T. Gai, J. Feng, K. Li, W. Zhang, Y. Li, F. Wang, D. Chao, Y. Wang, D. Zhao and W. Li, *J. Am. Chem. Soc.*, 2024, **146**, 15496-15505.
21 M. Xie, X. Lin, Z. Huang, Y. Li, Y. Zhong, Z. Cheng, L. Yuan, Y. Shen, X. Lu, T. Zhai and Y. Huang, *Adv. Funct. Mater.*, 2020, **30**, 1905949.
22 N. You, X. Liu, Q. Zhang, Z. Wang, J. Wang, Y. Xu, X. Li, Y. Guo and S. Wang, *Rare Met.*, 2024, **43**, 5362-5371.
23 Y. Liu, K. Wang, X. Xu, K. Eid, A. M. Abdullah, L. Pan and Y. Yamauchi, *ACS Nano*, 2021, **15**, 13924-13942.
24 Y. Chen, S. Zhang, Y. Chen, H. Ding, S. Yao, Y. Tang, Z. Qiu, K. Xu, Y. Hu, H. Gong, Y. Hu and H. Pang, *Nano Res.*, 2025, **18**, 94907446.
25 X. Li, Y. Li, X. Zhao, F. Kang and L. Dong, *Energy Storage Mater.*, 2022, **53**, 505-513.
26 F. Sun, X. Liu, H. B. Wu, L. Wang, J. Gao, H. Li and Y. Lu, *Nano Lett.*, 2018, **18**, 3368-3376.
27 X. Dong, Y. Yang, B. Wang, Y. Cao, N. Wang, P. Li, Y. Wang and Y. Xia, *Adv. Sci.*, 2020, **7**, 2000196.
28 S. Xu, Y. Wen, Z. Chen, N. Ji, Z. Zou, M. Wu, L. Qu and J. Zhang, *Angew. Chem. Int. Ed.*, 2021, **60**, 24505-24509.
29 J. Ma, S. Xing, Y. Wang, J. Yang and F. Yu, *Nano-Micro Lett.*, 2024, **16**, 143.

View Article Online
DOI: 10.1039/D5CC02629F

Data availability

The data supporting this article have been included as part of the Supplementary Information.